Heterodyne transverse velocimetry for pressure-shear plate impact experiments

Christian Kettenbeil, Michael Mello, Moriah Bischann, and Guruswami Ravichandran

Citation: Journal of Applied Physics **123**, 125902 (2018); doi: 10.1063/1.5023007
View online: https://doi.org/10.1063/1.5023007
View Table of Contents: http://aip.scitation.org/toc/jap/123/12
Published by the American Institute of Physics

JOURNAL OF APPLIED PHYSICS **123**, 125902 (2018)

Heterodyne transverse velocimetry for pressure-shear plate impact experiments

Christian Kettenbeil,[a] Michael Mello, Moriah Bischann, and Guruswami Ravichandran
Division of Engineering and Applied Science, California Institute of Technology, 1200 E. California Blvd., Pasadena, California 91125, USA

(Received 19 January 2018; accepted 10 March 2018; published online 29 March 2018)

Pressure-shear plate impact experiments have traditionally relied on free space beam interferometers to measure transverse and normal particle velocities at the rear surface of the target plate. Here, we present two different interferometry schemes that leverage heterodyne techniques, which enable the simultaneous measurement of normal and transverse velocities using short-time Fourier transforms. Both techniques rely on diffracted 1st order beams that are generated by a specular, metallic grating deposited on the rear surface of the target plate. The diffracted beam photonic Doppler velocimetry technique interferes each 1st order beam with a reference of slightly higher wavelength to create a constant carrier frequency at zero particle velocity. The second technique interferes the 1st order beams with each other and employs an acousto-optic frequency shifter on the +1st order beam to create a heterodyne transverse velocimeter. For both interferometer techniques, the 0th order beam is interfered in a heterodyne photonic Doppler velocimetry arrangement to obtain a measurement of the normal particle velocity. An overview of both configurations is presented along with a derivation of the interferometer sensitivities to transverse and normal particle velocities as well as design guidelines for the optical system. Results from normal impact experiments conducted on Y-cut quartz are presented as the experimental validation of the two proposed techniques. *Published by AIP Publishing.*
https://doi.org/10.1063/1.5023007

I. INTRODUCTION

The measurement of plane waves involving both longitudinal and transverse velocity components is of particular importance for the study of material strength at high strain rates ($>10^4$ s^{-1}) and pressures ranging from hundreds of MPa to several TPa. These conditions arise in, among others: pressure-shear plate impact (PSPI) experiments,[1] dynamically loaded anisotropic crystals,[2,3] laser-generated shear waves,[4] and magnetically applied pressure-shear experiments (MAPS).[5] Traditional PSPI experiments rely on the transverse displacement interferometer (TDI)[2] for the measurement of in-plane displacement histories. Recently, this technique has been extended to an all fiber-optic configuration.[6] Alternative schemes have leveraged dual VISAR (Velocity Interferometer System for Any Reflector) arrangements[3] that utilize normal and angled probes to measure transverse velocity components. The main disadvantage of this technique is that the fringe constant, as determined by the etalon delay leg, is set to measure a superposition of both normal and transverse particle velocities which generally differ by an order of magnitude. Hence, the dual VISAR approach cannot realize the full potential of the VISAR interferometry technique for PSPI experiments.

In recent years, there has been a paradigm shift towards the application of PDV (photonic Doppler velocimetry) for normal velocity measurements.[7] Along with the change in instrumentation came the utilization of robust short-time Fourier transform analysis techniques that are inherently more immune to signal noise than previously used phase-based methods and can therefore tolerate more light loss during an experiment. The frequency-based approach is also largely immune to amplitude modulation of the interferometer signals and does not depend on normalized (amplitude corrected) fringe records to extract frequency information, as required when processing a single (unheterodyned) interferometer signal.

A limitation of "standard" (unheterodyned) PDV is the inability of the technique to derive temporally resolved measurements of low particle velocities from fringe records or even partial fringes with correspondingly low signal frequencies. This limitation in temporal resolution leads to inaccuracies and signal processing artifacts as demonstrated by the discrepancy between a synthetic ramp velocity input pulse and its measured result depicted in Fig. 1(a). A heterodyned interferometer signal exhibits a carrier frequency f_c at zero target velocity as depicted by the ramp wave frequency spectrum in Fig. 1(b). The increased frequency enables the use of shorter time windows for the Fourier analysis and thus provides a high temporal resolution even at low velocities. While information at low velocities is not always required for traditional normal plate impact experiments, it is absolutely crucial for measuring transverse velocities in PSPI experiments, which are typically below 50 m/s.

The main goal of this work is to extend heterodyne PDV techniques, with their robust frequency-based analysis methods, to transverse interferometers utilized in PSPI[1] and magnetically applied pressure-shear experiments.[5] Two different approaches were pursued to introduce a carrier frequency in transverse velocimetry signals. Both techniques rely on

[a]Electronic mail: ckb@caltech.edu

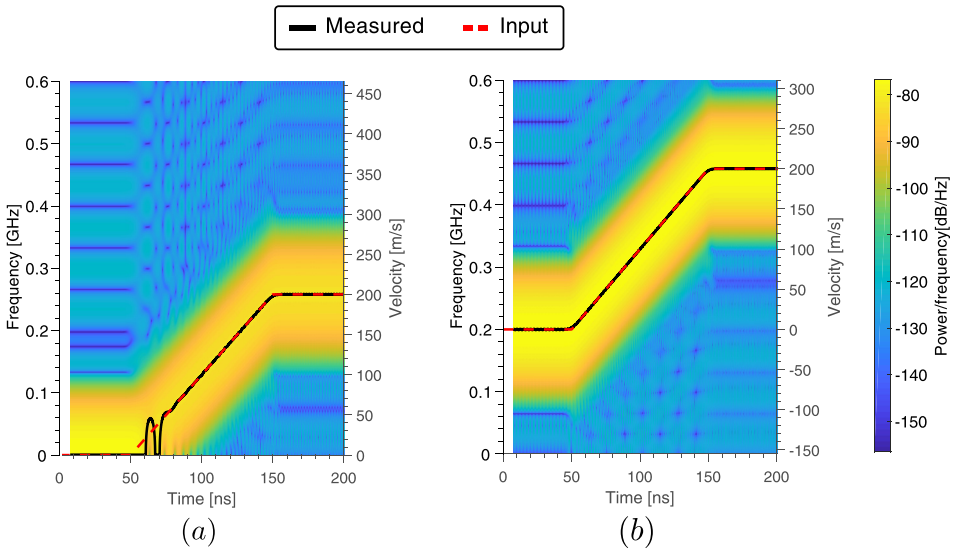

FIG. 1. Frequency spectrum over time for a ramp velocity input pulse (dashed line) with inferred velocity for (a) "standard" and (b) heterodyne PDV. A Hamming window with a duration $\tau = 15$ ns was employed for the frequency analysis.

diffracted 1st order beams generated by a specular, metallic grating deposited on the rear surface of the target plate. The diffracted beam photonic Doppler velocimetry (DPDV) technique interferes each 1st order beam with a reference laser adjusted to a slightly higher wavelength. An additional benefit of this transverse velocimeter lies in the independent measure of the normal velocity record that can be obtained by decoupling the normal motion from the diffracted order signals. The second technique, called the heterodyne transverse velocimeter (HTV), sends the +1st diffracted order through an acousto-optic frequency shifter to create a carrier frequency upon interference with the –1st order beam. In a similar fashion to the transverse displacement interferometer,[2] this approach provides a pure measurement of transverse motion. A measurement of the normal particle velocity is obtained from a heterodyne PDV arrangement employing the reflected 0th order diffracted beam. The strengths and limitations of each interferometer design are addressed and the techniques are compared by examining fringe records obtained from normal impact validation experiments conducted on Y-cut quartz.

II. OPTICAL DESIGN

Collecting diffracted or scattered light at an angle from the surface normal, to measure in-plane transverse displacements or velocities, poses a set of unique challenges in PSPI experiments that are not encountered in normal plate impact experiments. Normal displacement accumulated over the course of the experiment causes decentering of the diffracted beams at the receiving fiber-optic probes resulting in a rapid loss of light intensity. Light loss is further exacerbated by small tilt angles between the impacted surfaces of the flyer and target plates. Analyzing the geometrical effects of target tilt and normal displacement of the target surface can provide valuable insights into a suitable optical design. The optical design software Zemax was applied to investigate and quantify light loss due to both of these effects during PSPI experiments. The normal displacement during a PSPI experiment will depend on the impact velocity, experiment duration, and material response, resulting in varying optimal designs for different experiments. However, impact tilts of up to 2 mrad (0.11°) are considered typical in PSPI experiments and should lie within the light loss tolerance exhibited by the optical system.

A. Probe design

Figure 2 shows two optical systems that were investigated for their tolerance to normal displacement and tilt of the target plate's rear surface. The calculation of the coupling efficiency requires the computation of an overlap integral between the electric field that impinges on the fiber-optic core and the mode that can propagate in the utilized single mode (SM) fiber. However, many qualitative trends can be explained by appealing to geometrical optics.

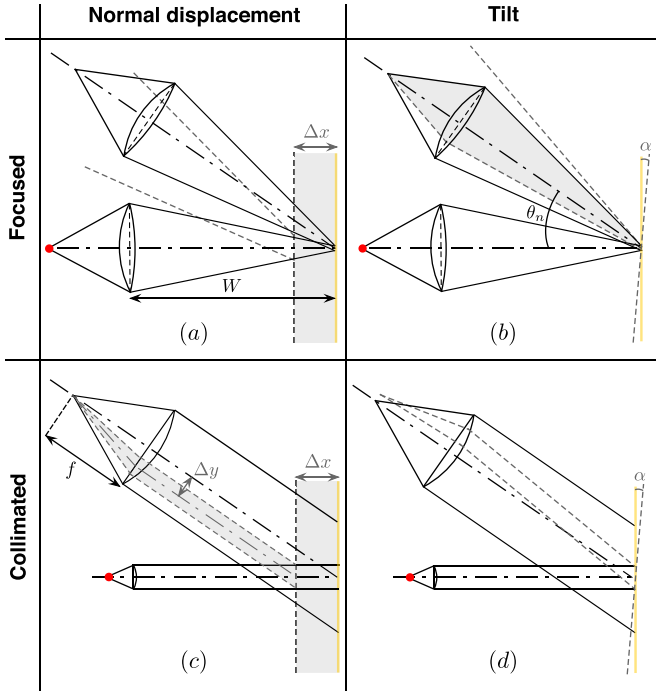

FIG. 2. Geometrical analysis of light coupling in fiber-optic transverse interferometers for focused (a) and (b) and collimated (c) and (d) optical designs subject to normal displacements Δx and tilt α.

1. Geometrical analysis of optical system

Figure 2(a) shows a fiber-optic configuration using focusing probes, which are commonly utilized in normal plate impact experiments.[8] The advantage of a focused optical system is its insensitivity to small rotations of the target rear surface, as highlighted in Fig. 2(b). The limitations of using this approach for transverse measurements become immediately apparent in Fig. 2(a), which highlights how quickly a diffracted or scattered beam is decentered with respect to the optical axis of the receiving probe upon normal motion of the target. Figure 2(a) also indicates that a larger spot size on the target rear surface, corresponding to a longer working distance W, increases the tolerance to normal displacement. The natural extension of this principle is to introduce a collimated light system, which is shown in Fig. 2(c). By reducing the beam diameter of the source probe, the diffracted beam will decenter, with respect to the optical axis of the receiving probe, without a reduction in light intensity at the fiber core until the decentered beam is vignetted by the edge of the receiving lens. The disadvantage of a collimated optical system is emphasized in Fig. 2(d). Any tilt angle α of the target rear surface will introduce a lateral translation of the focused spot αf from the fiber-optic core, which has a diameter of $8.2\,\mu$m for standard $\lambda = 1550$ nm wavelength single-mode fiber. One way to alleviate this concern is to utilize a source probe lens with a short focal length f resulting in a small source beam diameter. This leads to an enlarged focused spot size at the focal point of the receiving probe, which is larger than the fiber-optic core resulting in light coupling even when the center of the light distribution is displaced laterally by αf. This approach of increasing the system's tolerance to tilt comes at the expense of lower overall coupling efficiency. However, this does not pose a limitation for the systems presented here, as light collected by the angled probes is close to the damage threshold of the photodetectors, which limits the usable light intensity in the employed interferometer systems. Another factor that has to be taken into account with collimated optical systems is that a light beam can only stay collimated over a finite distance. Assuming Gaussian beam propagation, the collimation distance corresponds to the confocal parameter b, given by[9]

$$b = 2z_R = \frac{2\pi\omega_0^2}{\lambda}, \tag{1}$$

where z_R is the Rayleigh range parameter and ω_0 represents the beam waist radius. Equation (1) highlights the increasing importance of the Rayleigh range with smaller beam sizes. The collimated source beam used in the final experimental configuration has a beam diameter of $280\,\mu$m, which yields a Rayleigh range $z_R \approx 40$ mm, corresponding to an 80 mm collimation distance. In order to avoid reductions in coupling efficiency, the distance between the source and receiving lens should be kept below this value. In contrast to focusing systems, collimated designs experience no light loss due to the depth of field of the employed probe lenses for $W < z_R$.

Now that the geometrical effects have been established, the conflicting nature of the requirements for designs that accept large tilt angles and have a high tolerance to normal motion of the target plate becomes evident. A short focal length of the receiving lens will yield an increased tolerance to tilt, while a receiving lens with a long focal length will result in an increased tolerance to decentering from the accumulated normal displacement.

2. Optical simulations

Further progress towards the optical design requires a more quantitative comparison of several optical configurations. Optical simulations that propagate electric fields (Zemax Physical Optics Propagation feature) were carried out to compute the fiber coupling efficiency for varying amounts of normal displacement and target tilt. The fiber-optic lenses for the optical simulations were chosen based on typical PDV probes used for normal plate impact experiments.[8] Geometrical and optical properties of aspheric lenses with a focal length of $f = 1.4$ mm, 6.2 mm, and 11 mm were sourced from Thorlabs and used as input for the optical simulations. Focusing probes were modeled by a collimator pair of $f = 6.2$ mm aspheric lenses for which the spot size at the rear target surface was minimized by adjusting the spacing of the lenses along the optical axis.

The coupling efficiencies between the source and the receiving side probes for two focused and two collimated optical configurations are shown in Fig. 3. Focused designs are characterized by their working distance W, whereas collimated designs are designated by their source and receiving probe lens focal length f. The final coupling efficiency for each receiving side probe can be obtained by multiplying the results displayed in Fig. 3 by the diffraction efficiency I_n, which depends on the diffraction grating design and is described in Sec. II B. Figure 3(a) shows, as mentioned in the previous geometrical analysis, that focusing probes will suffer from a rapid loss of coupling efficiency upon normal motion of the target. Considering the immense light loss of the $W = 100$ mm focused design, it is not advisable to use working distances at or below this value for passive receiving probes. Figure 3(a) confirms that a focused configuration with a larger working distance W is less sensitive toward normal displacements of the target. As expected, the light loss designed into the collimated configurations yields a lower initial coupling efficiency. However, the small relative change of efficiency with target normal motion makes the collimated configuration more suited to transverse interferometry applications. Typical diagnostic systems can compensate the lower initial coupling efficiencies with a higher source beam intensity.

The importance of achieving a low impact tilt during PSPI experiments with spectrally reflective surfaces is demonstrated in Fig. 3(b). As previously mentioned, especially short focal length focused configurations offer a higher tolerance to tilt than collimated systems. However, Fig. 3(b) confirms the result of the geometric analysis that using a short focal length source lens in a collimated system can provide a suitable tilt tolerance, which can surpass the absolute efficiency of a $W = 250$ mm focused systems at tilt angles above 1.5 mrad (0.085°) and provide a much more constant light coupling. As a result of this analysis, a probe design that incorporates a $f = 1.4$ mm collimated source lens with a $f = 6.2$ mm receiving

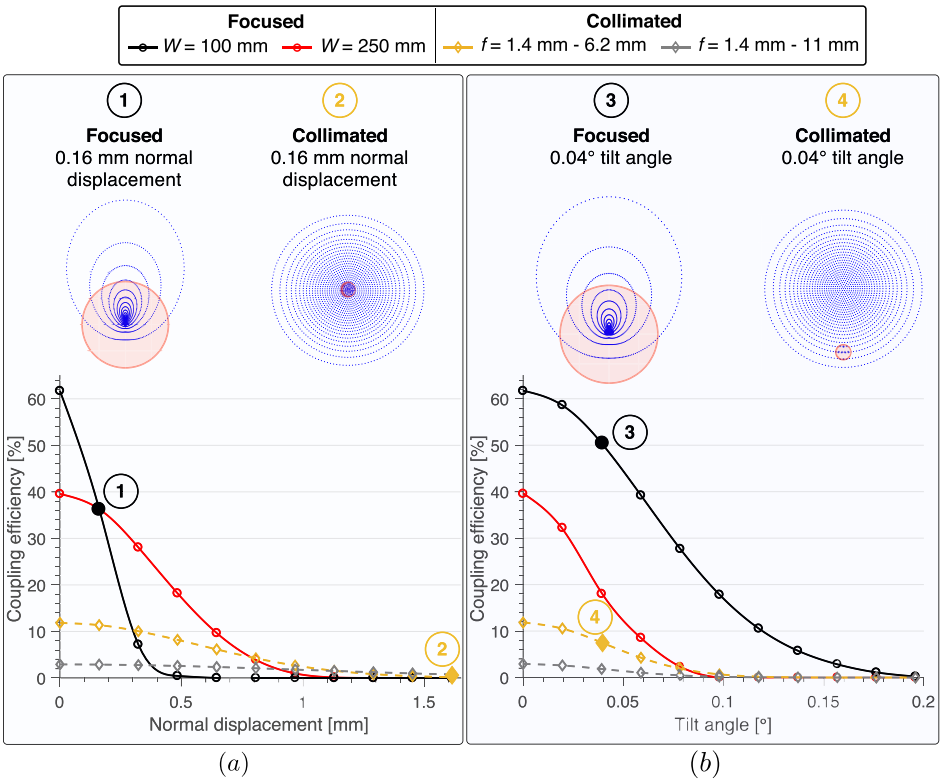

FIG. 3. Optical simulation results in relation to (a) normal displacement and (b) tilt angle for focused and collimated fiber-optic designs with corresponding spot diagrams superimposed on the 8.2 μm diameter single-mode fiber (red circle).

lens was selected, resulting in a collimation distance of 80 mm and a beam diameter of 280 μm. The optimized probe design provides sufficient spatial resolution for most PSPI experiments.

In summary, the small relative change of coupling efficiency demonstrated by the collimated beam configuration (even as the target surface is normally displaced) suggests that collimating probes are more suitable for transverse velocimetry applications. The relatively low coupling efficiencies do not restrict the light available to the interferometer as ample laser power is available to obtain a diffracted light intensity, which is close to the damage threshold of the interferometer system.

B. Grating design

A suitably designed diffraction grating can provide a high intensity beam at diffraction angles θ_n in a range of $0^\circ < \theta_n < 90^\circ$. In conjunction with an appropriate optical design, the diffraction intensity I_n provided by the diffraction grating can be designed such that no additional electric or optical amplification is required.

1. Diffraction angle

The diffraction angle is directly related to the resolution of the transverse velocity measurement. Assuming a normally incident source beam, the diffraction angle θ_n can be calculated by

$$d \sin(\theta_n) = n\lambda, \tag{2}$$

where d is the grating pitch, n is the diffraction order, and λ represents the wavelength of the incident light beam. The resolution of a transverse velocimetry diagnostic is defined here as the inverse of the interferometer sensitivity $S = d/2n$.[2,10] Hence, the highest resolution is obtained for the lowest grating pitch that still produces the $\pm n$th diffraction order, i.e., for $d = n\lambda$.

Increased diffraction angles will, however, promote decentering of the diffracted beams by a distance $\Delta y = \Delta x \sin\theta_n$ with respect to the optical axis of the receiving probes, as previously addressed and depicted in Fig. 2(c). The maximum normal displacement Δx that is acceptable for a successful measurement of transverse motion derived from the diffracted beams will thus be restricted. As a first order approximation, the accumulated normal displacement during a symmetric PSPI experiment can be estimated based on the observation time window T and the normal component of the impact velocity $V_0 \cos(\psi)$, where ψ is the inclination angle of the target and flyer plate relative to its direction of travel, by $\Delta x = V_0 \cos(\psi) T$. Considering an observation time window T, increased impact velocities V_0 will thus result in larger decentering values Δy leading to more challenging requirements for PSPI experiments at high impact velocities.

As discussed in Sec. I, the acceptable degree of light loss or corresponding reduction in contrast of the interference signal will depend on the method of analysis, i.e., if the velocity record is obtained from analyzing signal phase or frequency. Optical simulations of the collimated probe configuration used in this study ($f = 1.4$ mm source probe, $f = 6.2$ mm receiving probe), reveal that diffracted beam decentering values of Δy of 0.41 mm, 0.63 mm, and 0.75 mm will result in a light loss of 50%, 80%, and 90%, respectively. Decentering values assumed in the analysis are strictly attributed to normal displacement of the target rear surface and are independent of tilt. The corresponding

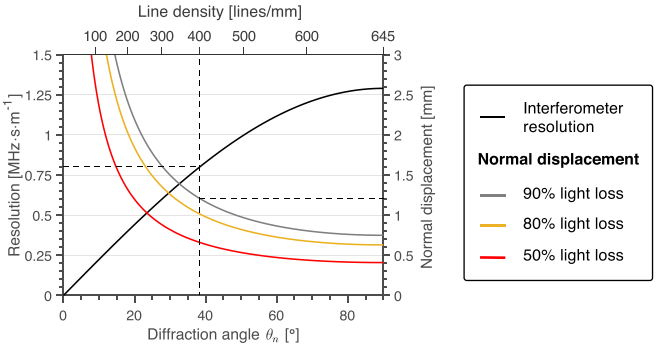

FIG. 4. Plot of the transverse interferometer resolution and maximum normal displacement, assuming the previously described optical system, for different light loss thresholds as a function of diffraction angle θ_n.

amount of normal displacement associated with the 50%, 80%, and 90% light loss levels varies with the diffraction angle (or grating line density) as summarized by the colored curves in Fig. 4. The black curve in the figure represents the measurement resolution (as previously defined). A suggested method for interpreting the curves in Fig. 4 is to estimate the maximum normal displacement (right vertical axis) that is accumulated during the observation time T of the experiment and find the intersection with the colored curves designating the acceptable degree of light loss considering the employed analysis technique. The corresponding diffraction angle (lower horizontal axis) or grating line density (upper horizontal axis) will then determine the maximum measurement resolution (left vertical axis). A diffraction grating with a pitch of $d = 2.5\ \mu$m ($\theta_1 = 38.32°$), highlighted in Fig. 4, was chosen for the experiments conducted in this study. This configuration provides a transverse velocity resolution of 0.8 MHz s m^{-1} and will experience a light loss of 90% at a normal displacement of 1.2 mm.

2. Diffraction intensity

In addition to selecting the desired diffraction angle θ_n, the structure of the grating can be designed to obtain a desired intensity distribution into each diffraction order. For the purpose of this study only binary, reflective diffraction gratings, as shown in Fig. 5(a), were considered. For this case, the grating structure $l(x)$ can be represented by the following aperture function:

$$l(x) = \begin{cases} e^{i\phi_1} = e^{i4\pi n_0 h/\lambda} & 0 \le x \le \beta d \\ e^{i\phi_2} = 1 & \beta d < x < d, \end{cases} \tag{3}$$

where ϕ_1 and ϕ_2 are phase terms associated with optical path length (OPL), n_0 is the refractive index of the medium that the incident light propagates in, h represents the step height, and β is the duty cycle of the diffraction grating.

According to the Fraunhofer diffraction theory,[11] the intensity I_n of the nth order diffracted beams resulting from a unity amplitude plane wave directed at normal incidence to the grating is given by the absolute square of the Fourier transform of the aperture function $l(x)$ and can be expressed as

$$I_n = \left| \int_0^{\beta d} e^{i\phi_1} e^{-2\pi i n x/d} dx + \int_{\beta d}^{d} e^{i\phi_2} e^{-2\pi i n x/d} dx \right|^2, \tag{4}$$

resulting in a 0th order diffraction intensity of

$$I_0 = 2\beta^2 \left(1 + \cos\left(\frac{4\pi n_0 h}{\lambda}\right)\right), \tag{5}$$

and a diffraction intensity of the first order beams given by

$$I_1 = \frac{1}{\pi^2}\left(1 - \cos\left(\frac{4\pi n_0 h}{\lambda}\right)\right)(1 - \cos(2\pi\beta)). \tag{6}$$

Equation (6) reveals that a duty cycle of $\beta = 0.5$ results in the highest intensity for the ± 1st order diffracted beams. In anticipation of pronounced light loss by the angled fiber-optic probes, more light should be directed into the ± 1st order diffracted beams. The diffraction grating selected for this study has a duty cycle of $\beta = 0.5$ and a grating height of $h = 320$ nm resulting in a 0th order efficiency of 7.3% and a 1st order efficiency of 37.6% in both diffracted beams as highlighted by the intersections of the dashed black lines in Fig. 5.

The light response from the diffraction grating was further tailored for this study to increase the tolerance of the optical system to target tilt. This objective was achieved by designing a grating structure with slightly broadened diffraction lobes centered around the primary diffraction angle θ_1. Broadened lobes will thus contribute light to the fiber optic probe even as the diffracted beam is slightly inclined due to tilt induced rotation of the target rear surface. The novel

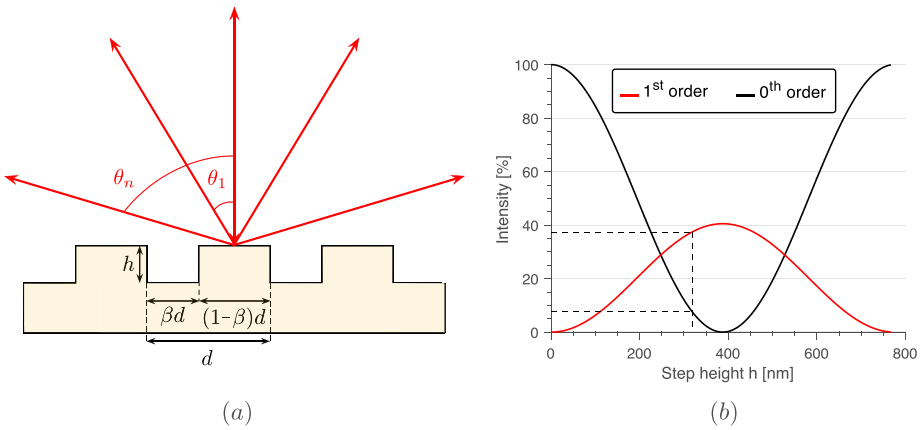

FIG. 5. (a) Structure of a reflective binary diffraction grating and (b) its diffracted beam intensity as a function of step height h for a duty cycle β of 0.5.

grating structure has a varying pitch that steps from $d_h^i = 2.45\ \mu$m to $d_h^i = 2.55\ \mu$m in 5 nm increments as depicted in Fig. 6(a). The varying pitch results in a corresponding range of diffraction angles $\theta_1 = 38.3 \pm 0.9°$ per Eq. (2). The feature width βd was varied accordingly to maintain a constant duty cycle of $\beta = 0.5$.

Furthermore, the diffracted lobes were also slightly broadened in the direction lying perpendicular to the primary diffraction plane to obtain an increased tolerance to tilt in the orthogonal plane as well. Broadened diffraction lobes in the orthogonal direction were achieved by superimposing a coarse cross grating structure with a pitch of $d_v = 80\ \mu$m and a duty cycle of 0.2, oriented perpendicular to the fine grating structure as shown in Fig. 6(a). The design freedom afforded by the e-beam lithography technique, which is used to manufacture the grating structure, entails that only a new pattern drawing has to be created to generate the aforementioned modifications.

III. HETERODYNE TRANSVERSE INTERFEROMETRY

Two new and novel applications of heterodyning interferometer signals for transverse velocity measurements are described in Secs. III A and B. The light beams with different wavelengths are created by using either a wavelength-tunable laser as a stationary reference beam or an acousto-optic frequency shifter that is applied to the +1st order diffracted light beam.

A. Diffracted beam photonic Doppler velocimetry

1. Interferometer design

The first approach is the fiber-optic DPDV arrangement, which is comprised of the drive, reference, and sensing groups as depicted in Fig. 7. The drive group hardware elements include a seed laser with an adjustable center wavelength between 1550 nm and 1570 nm, an Erbium doped 2 W booster stage, a 1×2 fiber-optic splitter, circulators (high-power model for 0th order), attenuators, and fiber-optic collimating probes. PDV fiber-optic probes illuminate the leading edge of the sabot and rear surface of the target plate as shown in Fig. 7 and collect normally scattered and reflected light from each respective surface. A pair of DPDV "side probes" collect the symmetrically diffracted beams. The 0th order beam and the scattered light from the sabot are passed through a fiber-optic circulator, and all collected beams are redirected to variable attenuators before propagating to the sensing group elements as depicted in Fig. 7. Reference group hardware elements depicted in Fig. 7 generate the reference beams, which are interfered with the four collected drive group source beams. The reference light is produced by a fiber laser with an adjustable center wavelength between 1535 nm and 1580 nm and a power output of 40 mW. A reference beam wavelength of 1550.017 nm was selected for the DPDV validation experiment, which generated a constant carrier signal frequency of 0.66 GHz at zero particle velocity when mixed with the source light with a wavelength of 1550.012 nm. Sensing group hardware elements, depicted in Fig. 7, interfere the collected return light with the reference light and convert the resulting interference signals into digitized fringe records for analysis. The four Drive Group source beams are combined into PDV/DPDV beam pairs using two 1×2 Single Mode (SM) fiber-optic couplers as shown. The diffracted light beams are each initially sent through a $4\ \text{km} \times 2$ Network Simulation Module, which delays each beam by $\approx 20\ \mu$s with respect to its PDV counterpart before the beams are combined. Each beam pair is

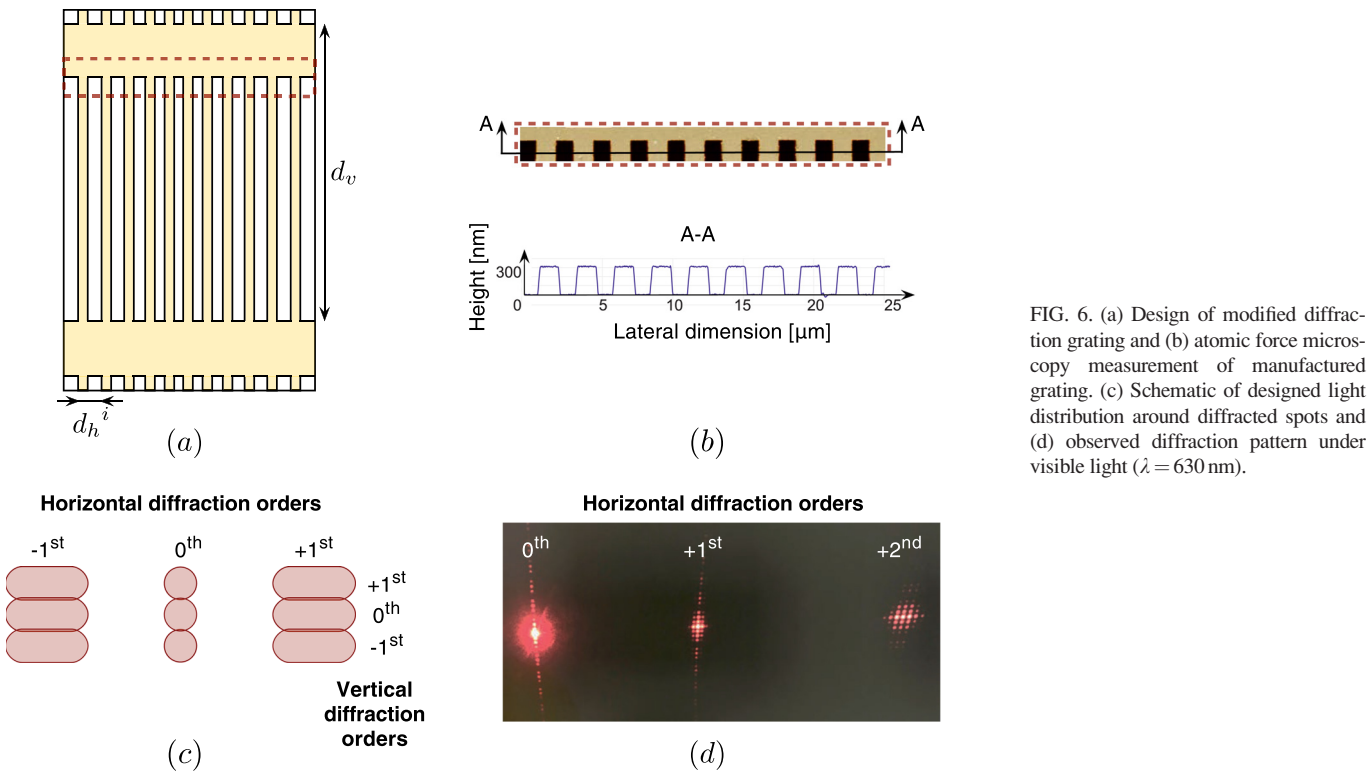

FIG. 6. (a) Design of modified diffraction grating and (b) atomic force microscopy measurement of manufactured grating. (c) Schematic of designed light distribution around diffracted spots and (d) observed diffraction pattern under visible light ($\lambda = 630$ nm).

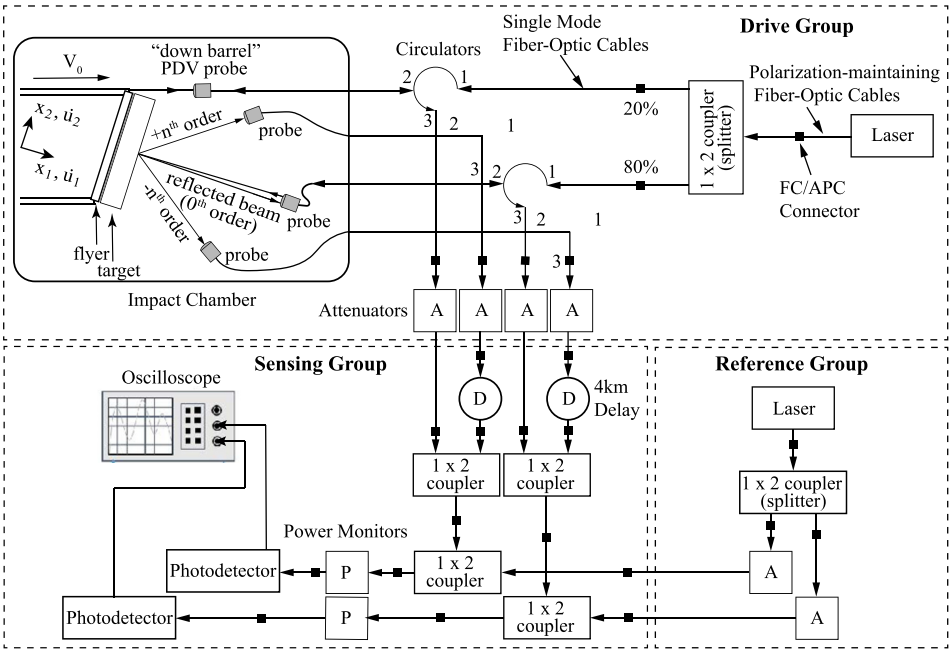

FIG. 7. Schematic of DPDV system for combined measurement of normal and transverse particle velocities in PSPI experiments.

then combined with a reference beam using a 1×2 SM fiber-optic coupler with a 10/90 coupling ratio. Interfering beam trains are each monitored by an in-line power monitor and terminate at a photodetector where the modulating light fields are converted into electrical signals. The time multiplexed PDV and DPDV interferometer signals are recorded using only 2-channels of a 4-channel oscilloscope to take advantage of the doubled sampling rate of 20 GSa/s.

2. Interferometer sensitivities

Figure 8 depicts the oblique impact between a flyer and target plate in a PSPI experiment along with the reflected (0th order) and symmetrically diffracted *n*th order beams produced by the diffraction grating at the rear surface of the target plate. The ray diagram on the right hand side of Fig. 8 graphically depicts the optical path length change (δOPL) experienced by a normally reflected (0th order) beam and a diffracted ($+n$th order) beam in response to infinitesimal normal and transverse displacements (δu_1, δu_2) of the target rear surface. The corresponding optical path length changes of the reflected and symmetrically diffracted $\pm n$th order beams are summarized in Fig. 8 under the assumption that the target rear surface

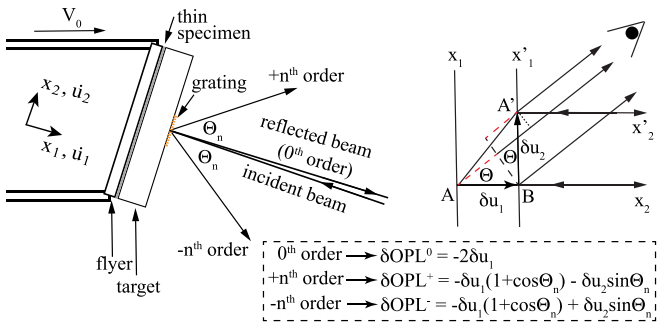

FIG. 8. Changes in optical path length (OPL) of the 0th order (reflected) and nth order diffracted beams due to small (positive), normal, and transverse displacements (u_1, u_2) of the target rear surface as point A displaces to A'.

displaced toward the detector as shown. The highly magnified optical ray diagram on the right of Fig. 8 shows parallel horizontal rays impinging upon points A and A', which represent two rays out of a multitude of such rays that comprise the incident collimated probe beam.

DPDV measurement sensitivity is derived by invoking the two beam, time-averaged intensity formula

$$I \propto (\vec{E}_S + \vec{E}_R) \cdot (\vec{E}_S + \vec{E}_R)^*, \tag{7}$$

where $\vec{E}_S$ and $\vec{E}_R$ are the electric field plane wave representations of the source and reference beams and the asterisk symbol denotes the complex conjugate operation.[2] Substituting for all time varying phase terms including those corresponding to changes in optical path length (OPL) of the $\pm n$th order diffracted beams, as shown in Fig. 8, leads to an expression for the time-averaged intensity of the heterodyned DPDV interference signals given by

$$I^{\pm}(t) = I_S^{\pm} + I_R^{\pm} + 2\sqrt{I_S^{\pm} I_R^{\pm}} \cos\left[\frac{2\pi}{\lambda_S}(u_1(t)(1-\cos\theta_n) \pm u_2(t)\sin\theta_n) + 2\pi(f_S - f_R)t - \phi^{\pm}\right]. \tag{8}$$

Here I_S and I_R represent the time-averaged steady state intensity of the source and reference beams, λ_S represents the wavelength of the source light, f_S and f_R are the optical frequencies of the source and reference light fields, and $\phi^{\pm}$ is an arbitrary constant phase in each interference signal. Application of a short-time Fourier transform algorithm to the recorded DPDV fringe records extracts the encoded signal frequencies corresponding to

$$f^{+}(t) = \frac{1}{\lambda_S}(\dot{u}_1(t)(1+\cos\theta_n) + \dot{u}_2\sin\theta_n) + (f_S - f_R), \tag{9}$$

$$f^{-}(t) = \frac{1}{\lambda_S}(\dot{u}_1(t)(1+\cos\theta_n) - \dot{u}_2\sin\theta_n) + (f_S - f_R), \tag{10}$$

where $\dot{u}_1(t)$ and $\dot{u}_2(t)$ correspond to the normal and transverse particle velocity components.

Subtracting the two DPDV signal frequencies given by Eqs. (9) and (10) and substituting for $\sin\theta_n$ from the grating Eq. (2) yield an expression for the transverse particle velocity in terms of the grating pitch (d), diffraction order (n), and the extracted signal frequencies given by

$$\dot{u}_2 = \frac{d}{2n}(f^+(t) - f^-(t)). \tag{11}$$

The frequency scaling factor $d/2n$ effectively represents the fundamental measurement sensitivity of the DPDV to changes in the transverse velocity and is equivalent to the sensitivity of a transverse displacement interferometer.[2] Using the $\pm$1st order beams from a 400 lines/mm grating in the current DPDV configuration results in a transverse velocity measurement sensitivity of 1.25 m/s/MHz.

Addition of the two DPDV signal frequencies given by Eqs. (9) and (10) yields an expression for the normal particle velocity in terms of the measured signal frequencies and the independently measured carrier frequency ($f_C = f_S - f_R$) given by

$$\dot{u}_1 = \frac{\lambda_S}{2(1+\cos\theta_n)}(f^+(t) + f^-(t) - 2f_C). \tag{12}$$

The scaling factor $\lambda_S/[2(1+\cos\theta_n)]$ represents the fundamental measurement sensitivity of the DPDV to changes in normal velocity. DPDV is evidently $(1+\cos\theta_n)$ times more sensitive to changes in normal velocity compared to a standard PDV, which has a sensitivity of $\lambda_S/2$.[7] Using the $\pm$1st order beams of a 400 lines/mm grating in the current DPDV configuration results in a normal velocity measurement sensitivity of 0.434 m/s/MHz, which represents a factor of 1.78 increase over the sensitivity of the PDV when using the 0th order beam at the same source wavelength.

3. Time uncertainty of signals

The uncertainty principle of signal processing, commonly referred to as the Heisenberg-Gabor limit,[12] given by

$$\Delta t \Delta f \geq \frac{1}{4\pi}, \tag{13}$$

imposes a restriction on how well both signal frequencies f and their location in time t can be resolved. By examining Eqs. (11) and (12) in this context, it becomes clear that adding or subtracting frequencies $f^{\pm}(t)$ that have an uncertainty about their position in time will introduce errors in determining the transverse $\dot{u}_2(t)$ and normal velocities $\dot{u}_1(t)$.

A synthetic example based on the analytical result of the Y-cut quartz validation experiment has been devised to demonstrate the issues arising from this approach. The ideal normal and transverse velocity records, with a rise time of 10 ns to transition between states, are depicted in Fig. 9(a). The velocity records are integrated over time to yield the corresponding displacements $u_1(t)$ and $u_2(t)$ that are subsequently inserted into Eq. (8) with a carrier frequency of $f_c = 1$ GHz to generate the synthetic light intensity signals $I^{\pm}$(t). An interferometer signal that more accurately reflects experimental results was generated by adding a noise term drawn from the standard normal distribution $\mathcal{N}(0,1)$ with a signal noise fraction of 10%

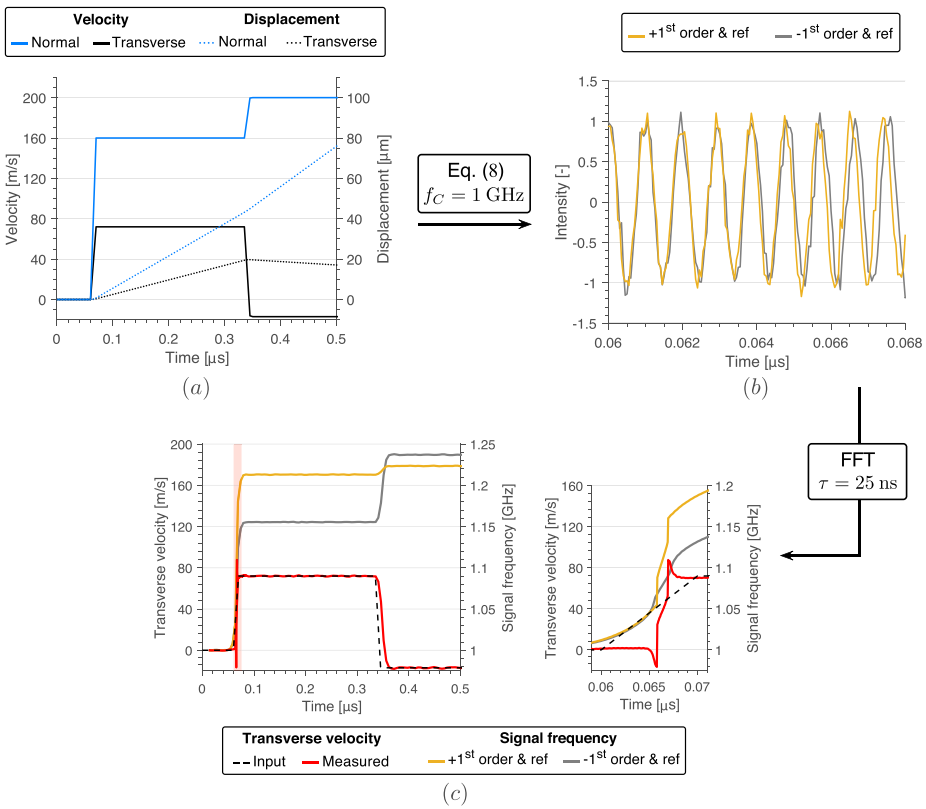

FIG. 9. Synthetic experiment highlighting the limitations of superimposing frequency signals due to their time uncertainty. (a) Theoretical velocity and displacement profiles of Y-cut quartz validation experiment. (b) Fringe patterns of diffraction orders interfered with a stationary reference beam of different wavelengths providing a carrier frequency of 1 GHz with a 10% noise fraction. (c) Result from frequency analysis with a 25 ns Hamming window, displaying artifacts during the QL wave transient associated with the superposition of frequency signals that are uncertain in time.

$$I^{\pm}_{noise}(t) = I^{\pm}(t) + 0.1\mathcal{N}(0,1)(t). \tag{14}$$

A short-time Fourier transform analysis with a $\tau = 25\,\text{ns}$ Hamming window was applied to the noise afflicted intensity signal generated by Eq. (14). Figure 9(c) shows the decoupled transverse $\dot{u}_2(t)$ and normal $\dot{u}_1(t)$ velocities that were calculated by Eqs. (11) and (12), respectively. It becomes evident that the velocity transient that coincides with the arrival of the first elastic wave gives rise to artifacts as shown in Fig. 9(c). These artifacts become more dominant for cases where the transverse velocity is orders of magnitude slower than the normal velocity, which is typical for PSPI experiments.

B. Heterodyne transverse velocimetry

1. Interferometer design

The second approach for designing a heterodyne transverse interferometer circumvents the issues related to the time uncertainty of frequency records, as discussed in Sec. III A, by optically decoupling the normal and transverse motion in a similar fashion to a transverse displacement interferometer.[2] The novelty of the HTV technique lies in the way it directly extracts the signal frequency through the use of robust frequency-based algorithms from a heterodyned transverse displacement interferometer, which by its very nature is purely sensitive to transverse motion. HTV is thus immune to signal artifacts that necessarily arise when frequency signals are added or subtracted to decouple motion components such as in the DPDV technique. That said, the DPDV technique has been shown to have the same sensitivity to transverse motion while offering increased sensitivity to normal motion compared to PDV. Each technique will thus have its advantages and disadvantages and it is left to the experimentalist to decide which technique to apply based on the experimental objectives and available instrumentation.

Many elements of the HTV interferometer are identical to the DPDV components. However, the HTV optical configuration shown in Fig. 10 relies on interference between the symmetrically diffracted $\pm$1st order beams, which leads to modifications of the DPDV arrangement displayed in Fig. 7. As depicted in Fig. 10, the +1st order diffracted beam is passed through the acousto-optic frequency shifter, which provides a frequency shift equal to the frequency of the acoustic wave propagating inside its tellurium dioxide window. An up-shift frequency of 300 MHz was chosen as it offers an acceptable amount of light attenuation and enables the use of $\tau \geq 5\,\text{ns}$ analysis windows, resolving transients with 10%–90% rise times of $t_R \approx 2\,\text{ns}$.[7] As previously mentioned, reducing τ further will lead to a higher frequency uncertainty, which is problematic for resolving the low transverse velocities observed in PSPI experiments.

2. Interferometer sensitivities

As depicted in Fig. 10, the HTV interferometer interferes the +1st and −1st diffracted order, which changes Eq. (8) to

$$I(t) = I_+ + I_- + 2\sqrt{I_+ I_-}\cos\left[\frac{2\pi}{\lambda_S}u_2(t)\sin\theta_n + 2\pi(f_+ - f_-)t - \phi\right]. \tag{15}$$

Equation (15) shows that the HTV scheme is insensitive to normal displacement and is therefore a pure transverse interferometer. Applying short-time Fourier transform analysis methods yields a signal frequency that is now directly related to the transverse velocity by

$$\dot{u}_2 = \frac{\lambda_S}{2\sin\theta_n}(f(t) - f_c) = \frac{d}{2n}(f(t) - f_c). \tag{16}$$

As expected, the fundamental sensitivity of the transverse displacement interferometer of $d/2n$ is recovered.

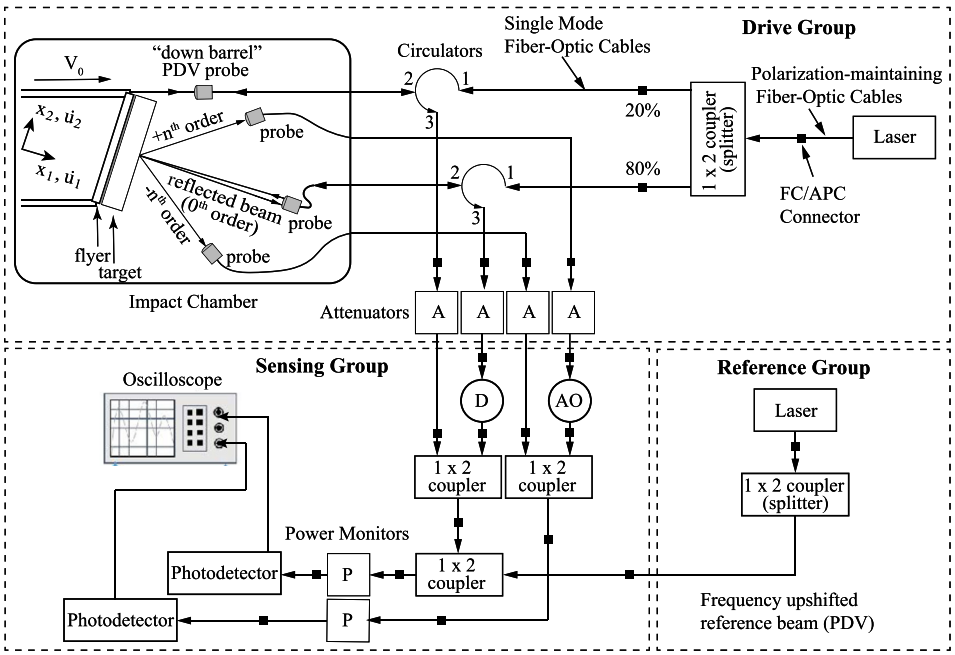

FIG. 10. Schematic of HTV system for combined measurement of normal and transverse particle velocities in PSPI experiments.

IV. EXPERIMENTAL VALIDATION

A. Wave propagation in anisotropic crystals

A historical benchmark experiment used in the validation of the transverse displacement[2] and velocity interferometers (dual VISAR)[3] is to conduct a normal plate impact on a Y-cut quartz target. Due to coupling of the shear and normal response of the anisotropic single crystal, both shear and pressure waves are generated by the normal impact. This experiment creates very challenging conditions for interferometry systems such as rapid transients and velocity reversals in the transverse velocity record.

An analytic solution to the wave propagation in anisotropic media can be derived from the linear-elastic wave equation given by

$$\rho \frac{\partial^2 u_i}{\partial t^2} = C_{ijkl} \frac{\partial^2 u_k}{\partial x_j \partial x_l}, \tag{17}$$

where C_{ijkl} represents the fourth rank elastic moduli tensor, u_i is the displacement in the three Cartesian coordinates x_i, and ρ is the material density. Before lateral release waves arrive at the measured material point, the displacement u_i can be represented by a plane wave $u_i = U_i f(t - p_m x_m/c)$ with an arbitrary function f of wave velocity c, a vector denoting the propagation direction p_m and a relative displacement U_i. By inserting this plane wave ansatz into Eq. (17), the following eigenvalue problem can be formulated:

$$(\Gamma_{ik} - \rho c^2 \delta_{ik}) U_i = 0, \tag{18}$$

where δ_{ik} is the Kronecker delta and Γ_{ik} represents the acoustic tensor, which is defined as

$$\Gamma_{ik} = C_{ijkl} p_j p_l. \tag{19}$$

The three eigenvalues of the acoustic tensor represent the product of the material density and the wave speed c_i for each corresponding eigenvector $\mathbf{U}^i$, which represent the polarization vectors of the three propagating waveforms. If no slip is assumed to occur during the experiment, the velocities and tractions are continuous across the flyer—target interface and the normal and transverse velocity—time profiles, given in Fig. 9(a), can be obtained. A more detailed description of elastic waves in anisotropic media can be found in Johnson.[13]

As shown in Fig. 11, only two waveforms can propagate given the described conditions. The polarization vector of the fast wave, commonly referred to as the quasi-longitudinal wave (QL), has its largest entry along the normal direction (y-axis of crystal), whereas the quasi-transverse wave (QT) is mainly polarized along the z-axis of the crystal.

B. Y-cut quartz normal impact experiments

Pressure-shear normal impact experiments were conducted using borosilicate glass flyer plates and single-crystal Y-cut quartz target plates as a means of validating the DPDV and HTV interferometry techniques. Single-crystal Y-cut quartz was selected as a target material because of the strong coupling exhibited between longitudinal and transverse particle motion under normal impact. The predicted sharp positive velocity jumps in the transverse and normal directions upon arrival of the QL wave followed by negative jumps upon arrival of the QT wave presented an ideal scenario for evaluating various attributes of the transverse interferometer systems such as the predicted interferometer sensitivities and the optical heterodyne feature for automatic, accurate detection of velocity reversals.

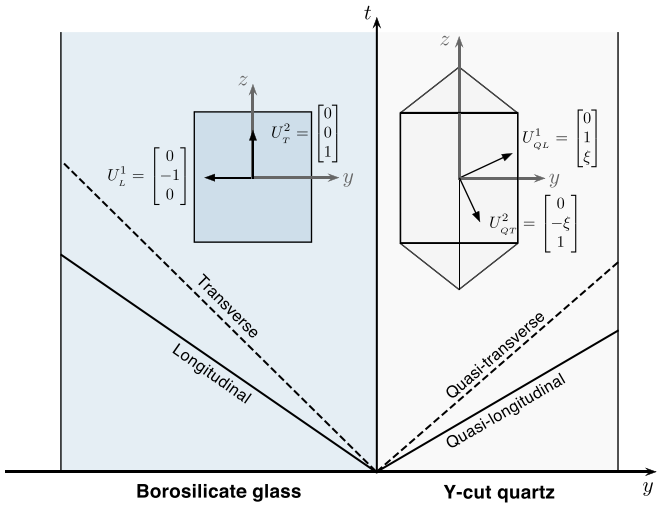

FIG. 11. X-t diagram of normal impact experiment with a borosilicate glass flyer plate and Y-cut quartz target plate with polarization vectors $\mathbf{U}^i$.

Cylindrical Y-cut quartz plates were obtained with a diameter of 30 ± 0.1 mm, a thickness of 5 ± 0.1 mm, and a Y-cut tolerance of $\pm 0.17°$. The target plate diameter was sufficiently large to provide an observation window of more than 2 μs before lateral release waves reached the center of the target. The circumference of the Y-cut quartz plate included a 5 mm long flat that was manufactured to be parallel to the z-axis of the quartz crystal. Values for density and stiffness coefficients were taken from the literature[14] and are as follows: density, $\rho = 2.65$ g/cm^3, $C_{22} = 87.16$ GPa, $C_{24} = 18.15$ GPa, $C_{44} = 58.14$ GPa, and $C_{66} = 40.26$ GPa.

The choice of borosilicate for the flyer plate material was based on three considerations: (a) choice of an isotropic material to simplify material alignment requirements, (b) a low acoustic impedance to generate relatively low stresses in both plates, and (c) sufficiently high yield strength in compression and shear to prevent premature failure of the flyer plate during the experiment. Cylindrical plates of Borofloat 33 glass were obtained with a diameter of 33.9 ± 0.1 mm and a thickness of 6.5 ± 0.1 mm. The flyer plate thickness was chosen to prevent wave reflections from the backside of the flyer plate from reaching the impact face prior to separation. Values for borosilicate material constants were obtained from Schott North America and are given as follows: density, $\rho = 2.2$ g/cm^3; elastic Young's modulus, $E = 64$ GPa; Poisson's ratio, $\nu = 0.2$.

A 400 lines/mm gold diffraction grating was fabricated onto the backside of each target plate using metal vapor deposition and electron beam (e-beam) lithography. The first manufacturing step consists of depositing a 20 nm chromium adhesion layer followed by a 250 nm thick gold reflective layer.

Gold exhibits very high reflectivity in the near infrared spectrum and does not suffer from oxidization, such as aluminum and silver. The creation of a high quality optical grating lends itself well to a lift-off process, which is typically conducted with a bi-layer resist. After alignment of the 5 mm flat edge with the coordinate system of the e-beam lithography tool, the desired grating pattern is exposed and the bi-layers are individually developed to create a well defined undercut resist profile. Subsequently, another gold layer of thickness $h = 320$ nm is deposited and residual resist features are dissolved, leaving an all gold diffraction grating on the target plate.

C. Experimental results

1. Error assessment

The accuracy of the velocimetry measurements is limited by the Heisenberg-Gabor limit [Eq. (13)], the exact knowledge of the source laser wavelength λ_S, the digitizer time calibration, and probe alignment to the designed angles.[15] Each probe alignment is conducted by maximizing the respective signal return. The cosine corrections of the PDV measurements, utilizing the 0th order diffracted beams, are assumed to be below 0.01%.[15] Considering the loss of coupling efficiency in the angled probes for tilt angles $\alpha > 0.5$ mrad, shown in Fig. 3, the uncertainty caused by small angle variations for the transverse velocimetry measurements is estimated to be below 0.08%. The uncertainty of the laser wavelength and the digitizer time measurement for these systems are typically below 10 ppm.[15] Based on these parameters, most of the uncertainty in velocimetry measurements is caused by identifying the peak frequency in the power spectrum of the short-time Fourier transform.[15]

The assessment of the frequency uncertainty in this study follows Dolan's approach,[7] which utilizes an analytically derived relation for the fitting of noise afflicted sinusoidal signals.[16] The resulting estimate of the frequency uncertainty Δf in a short-time Fourier transform analysis is based on the sampling frequency f_{sa} and the signal noise fraction σ of the velocimetry fringe records given by

$$\Delta f = \sqrt{\frac{6}{f_{sa}}}\frac{\sigma}{\pi}\tau^{-3/2}. \tag{20}$$

The signal noise fraction is estimated by[17]

$$\sigma^2 = \frac{1}{2}\frac{Bf_N}{\int |\tilde{S}(f)|^2 df - Bf_N}, \tag{21}$$

where B represents the mean (upper bound) noise level in the power spectrum of signal s(t) with its Nyquist frequency f_N and total area under its power spectrum $\int |\tilde{S}(f)|^2 df$.

The velocity uncertainty can then be deduced by multiplying the frequency uncertainty with the respective interferometer sensitivities

$$\Delta \dot{u}_i = S_i \sqrt{\frac{6}{f_{sa}}}\frac{\sigma}{\pi}\tau^{-3/2}, \quad i = 1, 2. \tag{22}$$

As previously mentioned, the sensitivities for PDV and DPDV/HTV measurements are given by $S_1 = \lambda_S/2$ and $S_2 = d/2n$, respectively. As the DPDV technique relies on two frequency measurements to obtain the transverse velocity profile $\dot{u}_2(t)$, the uncertainty associated with both results has to be considered. Corresponding uncertainty values, calculated by Eq. (22), were included in the results obtained for each validation experiment.

Equation (22) also highlights the importance of the window length τ for conducting precise frequency measurements. A trade-off between the velocity uncertainty and time resolution, approximated by the 10%–90% signal rise time $t_R \approx 0.37\ \tau$ (Hamming window function[7]), has to be taken into account for providing sufficient temporal resolution in the analysis of velocity time signals.

2. Diffracted beam photonic Doppler velocimetry measurements

Normal and transverse velocity profiles measured at the rear surface of the Y-cut quartz target plate using the DPDV diagnostic are plotted in Fig. 12. The velocity profiles were obtained from the acquired fringe records using a Hamming window duration of 50 ns with the window shifted one time step for every analysis (50 ps). The dashed lines represent the predicted velocity jumps of each respective motion component for a measured impact velocity of $V_0 = 211$ m/s. The

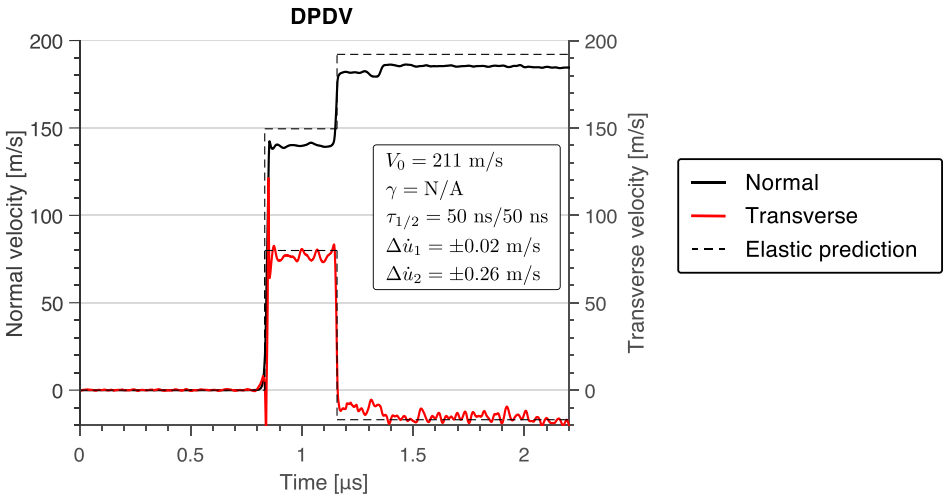

FIG. 12. Measured longitudinal and transverse velocity profiles with PDV/DPDV interferometer compared to predicted values based on the measured impact speed of $V_0 = 211$ m/s.

measured QL and final transverse QT velocity levels are in excellent agreement with theory, while the measured normal velocity jumps both fell 3%–4% short of their respective predicted values. Velocity measurements of the QL wave are sensitive to the impact tilt angle γ, but deviations in the final state can be attributed to uncertainty in the elastic stiffness constants used for the analysis. The tilt angle measurement was unsuccessful for this experiment; however, sufficient light return in the angled probes as well as velocity measurements that are close to the elastic predictions suggests an impact tilt γ below 2.5 mrad. As described previously, the time uncertainty of the DPDV signals leads to artifacts during velocity transients, which occur with the arrival of the QL wave, as shown in Fig. 12.

3. Heterodyne transverse velocimetry measurements

Figures 13(a) and 13(c) show a direct comparison of the fringe pattern observed during two different HTV experiments. The second experiment utilized a structured diffraction grating with slightly broadened diffraction lobes as described in Fig. 6. Due to a measured impact tilt of 2.2 mrad and distinct diffraction angles, the signal fringe contrast in the first experiment is reduced drastically with the arrival of the QL wave and almost vanishes with the appearance of the QT wave. In this region, only long window lengths of $\tau > 100$ ns can recover the transverse velocity information. However, the results of the second experiment, which utilized a structured grating, show an excellent fringe contrast even after the arrival of lateral release waves after 2.15 μs. Both the diffuse light response from the modified diffraction grating and a lower impact tilt value of 0.8 mrad contributed to maintaining a high coupling efficiency and hence a much improved fringe contrast. Comparing the spectrograms of both measurements in Figs. 13(b) and 13(d) illustrates the improvement in measurement uncertainty that is gained. Figures 13(b) and 13(d) reveal that the crystal axes in both experiments were oppositely oriented, which resulted in a reversed frequency response upon arrival of the QL and QT waves.

The measured normal and transverse velocities are depicted in Fig. 14. As previously discussed, no artifacts arise in the transverse velocimetry signals due to transients in the velocity profiles. Furthermore, the transverse velocity measurements vary considerably less around its respective steady-state value, indicating a more precise measurement compared to the DPDV result.[7] The transverse velocity profile matches the theoretical prediction very well, while the final state in the normal velocity profile is measured to be 3%–6% lower than the elastic prediction.

4. Orthogonality of polarization vectors

As previously discussed, the polarization vectors $\mathbf{U}^i$ are eigenvectors of the acoustic tensor. As the acoustic

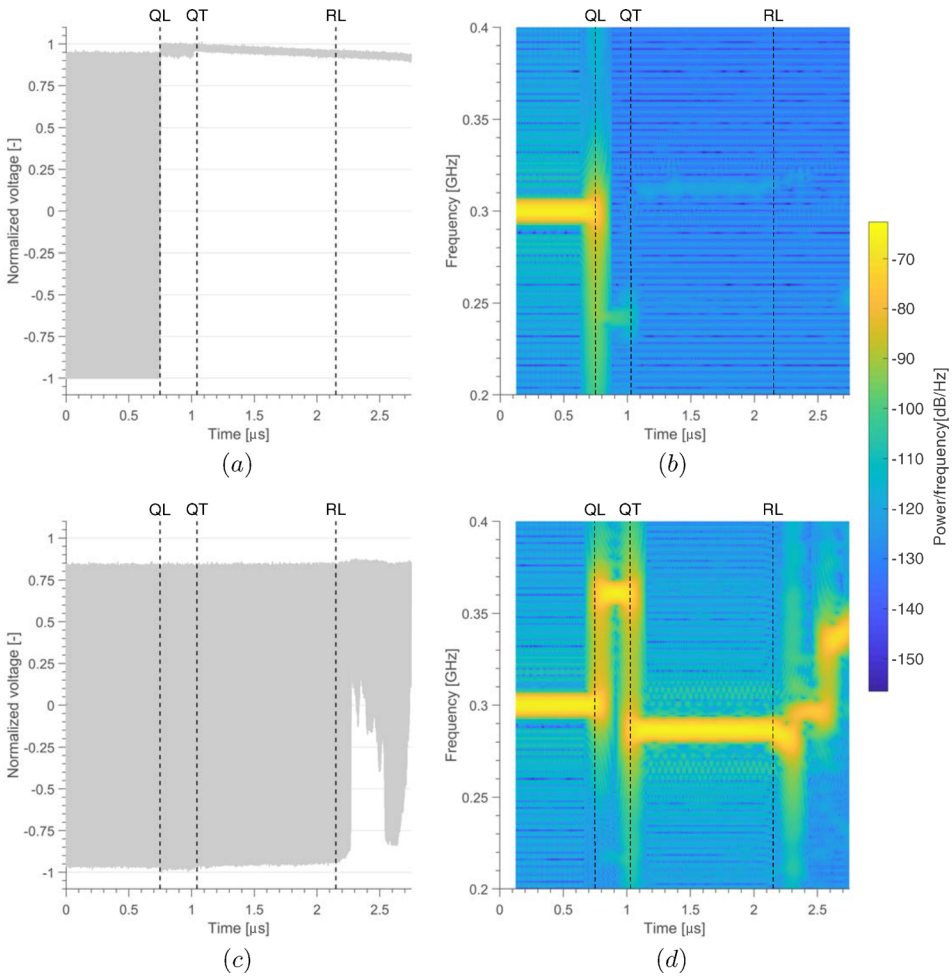

FIG. 13. Comparison of fringe pattern and resulting spectrogram ($\tau = 250$ ns) of the experiment with a standard (a) and (b) and modified diffraction grating (c) and (d) according to Sec. II B. QL, QT, and RL denote the arrival of the quasi-longitudinal, quasi-transverse and lateral release waves, respectively.

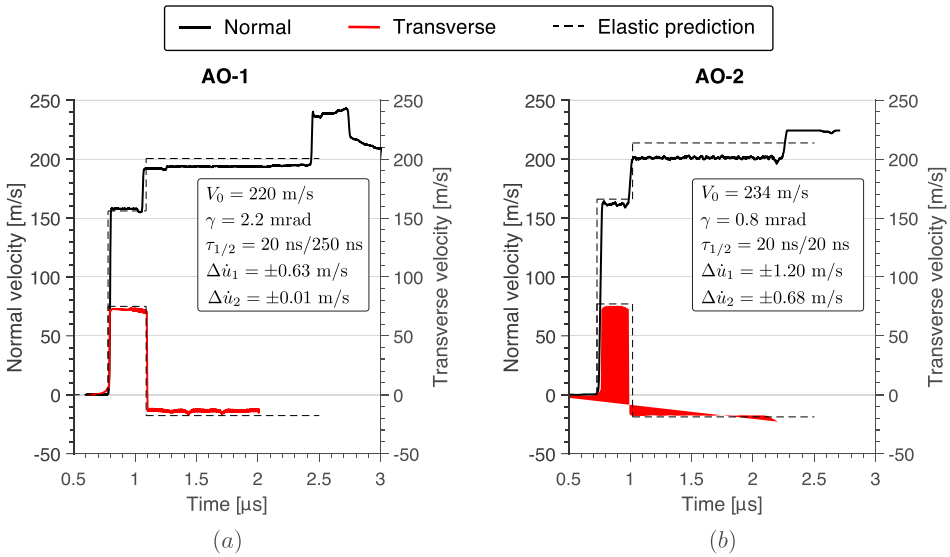

FIG. 14. Measured longitudinal and transverse velocity profiles compared to predicted values in (a) the experiment with the standard grating at an impact velocity of $V_0 = 220$ m/s and (b) the modified grating experiment with $V_0 = 234$ m/s.

tensor governing this problem is real and symmetric, it is guaranteed to have orthogonal eigenvectors. This property provides an additional opportunity to test the accuracy of the interferometer results by comparing the ideal orthogonality condition with the velocity jumps of the QL and QT waves.

The plot of transverse velocity $\dot{u}_2$ and longitudinal velocity $\dot{u}_1$ in Fig. 15 provides a graphical means of demonstrating this relationship and shows that the measured values of the transient and final velocity jumps are not perfectly orthogonal. The discrepancy mainly results from impact tilt, which affects the orientation of the polarization vectors. An impact with a tilt angle of 1.5 mrad (0.11°) and an impact velocity of $V_0 = 200$ m/s leads to an inclination of the propagating QL and QT waves to the y-axis of the quartz crystal of 2.6°, which is comparable to the observed deviation for the conducted experiments. The deviations from orthogonality are comparable for the HTV and DPDV experiments, with the slightly higher deviation in the DPDV experiments likely caused by a higher impact tilt angle γ. These values are, respectively, comparable to the 1.7° orthogonality deviation found by Kim and Clifton[2] in their study of transverse displacement interferometry with application to Y-cut quartz

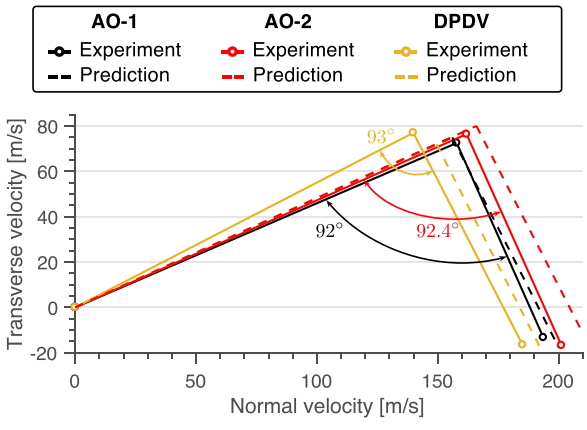

FIG. 15. Orthogonality of the measured velocity jumps during the arrival of the QL wave and QT waves.

in which a measured tilt value of 0.4 mrad and an impact velocity of $V_0 = 50$ m/s were observed.

V. CONCLUSION

In this work, two new heterodyne interferometry techniques for PSPI experiments are presented: DPDV and HTV. The novelty in both interferometers lies in a carrier frequency f_c that is superimposed on the transverse velocity signals. Application of robust frequency-based fringe processing algorithms enables accurate measurements of low velocities, with improved immunity to signal noise, and automatic detection of velocity reversals encountered in PSPI experiments. The DPDV technique provides an independent measure of normal particle velocity with an enhanced sensitivity compared to the PDV technique, but exhibits artifacts during rapid velocity transients, thus eliminating it from certain applications. The HTV technique does not suffer from the aforementioned issues and is therefore a superior transverse velocimeter, which manifests itself in more precise measurements. However, HTV is unable to provide additional information on the normal velocity record. The design and implementation of collimating fiber optic probes combined with structured diffraction gratings, engineered at the nano-scale, counteract coupling losses related to decentering and tilt of diffracted beams and effectively eliminate the need for additional electric or optical amplification. The validation impact experiments on Y-cut quartz showcased the efficacy of the optical design and interferometer techniques as challenging velocity transients and reversals were well resolved and showed good agreement with theoretical predictions.

These key developments will enable PSPI experiments at higher pressures (>25 GPa), which will ultimately enhance our understanding of material strength in extreme environments and across phase transformations. Although these developments are presented in the context of PSPI experiments, both heterodyne velocimetry techniques can be effectively used for measuring normal and transverse velocities associated with other dynamic phenomena, including laser driven shocks and magnetically applied pressure-shear loading.

ACKNOWLEDGMENTS

The authors are grateful for the support from the Office of Naval Research (Award No. N00014-16-1-2839) for the development of the PSPI capability at high pressures and the Air Force Office of Scientific Research (Award No. FA9550-12-1-0091) for the development of the PDV-DPDV interferometer system.

[1]R. W. Klopp, R. J. Clifton, and T. G. Shawki, Mech. Mater. **4**, 375 (1985).
[2]K. S. Kim, R. J. Clifton, and P. Kumar, J. Appl. Phys. **48**, 4132 (1977).
[3]L. C. Chhabildas, H. J. Sutherland, and J. R. Asay, J. Appl. Phys. **50**, 5196 (1979).
[4]J. Wang, N. R. Sottos, and R. L. Weaver, Exp. Mech. **43**, 323 (2003).
[5]C. S. Alexander, J. R. Asay, and T. A. Haill, J. Appl. Phys. **108**, 126101 (2010).
[6]B. Zuanetti, T. Wang, and V. Prakash, Rev. Sci. Instrum. **88**, 033108 (2017).
[7]D. H. Dolan, Rev. Sci. Instrum. **81**, 053905 (2010).
[8]T. Strand, R. Bonner, D. Hester, and T. Whitworth, in 3rd Annual PDV Conference (2008).
[9]A. E. Siegman, *Lasers* (University Science Books, 1986).
[10]M. Mello, C. Kettenbeil, M. Bischann, and G. Ravichandran, in *Shock Compression of Condensed Matter - 2017*, edited by R. Chau, T. Germann, and M. Lane. (American Institute of Physics, Melville, NY, 2018).
[11]G. Walze, Ph.D. thesis, Albert-Ludwigs-Universität Freiburg, 2005.
[12]D. Gabor, J. Inst. Elect. Eng. **93**, 429 (1946).
[13]J. N. Johnson, J. Appl. Phys. **42**, 5522 (1971).
[14]P. Heyliger, H. Ledbetter, and S. Kim, J. Acoust. Soc. Am. **114**, 644 (2003).
[15]B. J. Jensen, D. B. Holtkamp, P. A. Rigg, and D. H. Dolan, J. Appl. Phys. **101**, 013523 (2007).
[16]M. H. Montgomery and D. O'Donoghue, Delta Scuti Star Newsl. **13**, 28 (1999).
[17]D. H. Dolan and T. Ao, Release Notes for SIRHEN version 0.4, 2010.